sensors

MDPI

Article

Electrospun Nickel Manganite ($NiMn_2O_4$) Nanocrystalline Fibers for Humidity and Temperature Sensing

Milena P. Dojcinovic [1,*], Zorka Z. Vasiljevic [1], Jugoslav B. Krstic [2], Jelena D. Vujancevic [3], Smilja Markovic [3], Nenad B. Tadic [4] and Maria Vesna Nikolic [1]

1 Institute for Multidisciplinary Research, University of Belgrade, 11030 Belgrade, Serbia; zorkav@imsi.rs (Z.Z.V.); mariavesna@imsi.rs (M.V.N.)
2 Institute of Chemistry, Department of Catalysis and Chemical Engineering, Technology and Metallurgy, University of Belgrade, 11000 Belgrade, Serbia; jkrstic@nanosys.ihtm.bg.ac.rs
3 Institute of Technical Sciences of SASA, 11000 Belgrade, Serbia; jelena.vujancevic@itn.sanu.ac.rs (J.D.V.); smilja.markovic@itn.sanu.ac.rs (S.M.)
4 Faculty of Physics, University of Belgrade, 11000 Belgrade, Serbia; nenad.tadic@ff.bg.ac.rs
* Correspondence: milena.dojcinovic@imsi.rs

Abstract: Nickel manganite nanocrystalline fibers were obtained by electrospinning and subsequent calcination at 400 °C. As-spun fibers were characterized by TG/DTA, Scanning Electron Microscopy and FT-IR spectroscopy analysis. X-ray diffraction and FT-IR spectroscopy analysis confirmed the formation of nickel manganite with a cubic spinel structure, while N_2 physisorption at 77 K enabled determination of the BET specific surface area as 25.3 m^2/g and (BJH) mesopore volume as 21.5 m^2/g. The material constant (B) of the nanocrystalline nickel manganite fibers applied by drop-casting on test interdigitated electrodes on alumina substrate, dried at room temperature, was determined as 4379 K in the 20–50 °C temperature range and a temperature sensitivity of −4.95%/K at room temperature (25 °C). The change of impedance with relative humidity was monitored at 25 and 50 °C for a relative humidity (RH) change of 40 to 90% in the 42 Hzπ1 MHz frequency range. At 100 Hz and 25 °C, the sensitivity of 327.36 ± 80.12 kΩ/%RH was determined, showing that nickel manganite obtained by electrospinning has potential as a multifunctional material for combined humidity and temperature sensing.

Keywords: nickel manganite; electrospinning; nanocrystalline fibers; humidity sensing; temperature sensing; NTC thermistor

Citation: Dojcinovic, M.P.; Vasiljevic, Z.Z.; Krstic, J.B.; Vujancevic, J.D.; Markovic, S.; Tadic, N.B.; Nikolic, M.V. Electrospun Nickel Manganite ($NiMn_2O_4$) Nanocrystalline Fibers for Humidity and Temperature Sensing. *Sensors* **2021**, *21*, 4357. https://doi.org/10.3390/s21134357

Academic Editor: Olga Korostynska

Received: 29 April 2021
Accepted: 20 June 2021
Published: 25 June 2021

1. Introduction

Monitoring humidity and moisture levels is essential in many industrial processes, such as the food, medical and semiconductor industries, as high-quality products often need to be produced in controlled conditions [1]. Humidity sensors are components of smart monitoring systems [2]. In the food industry, besides humidity monitoring in the food production process, humidity sensors can be incorporated as components of intelligent food packaging [3]. Precision agriculture requires smart humidity sensors as part of a wireless sensor network [4,5], that includes monitoring of plant soil moisture essential for good plant growth [6,7]. Semiconductor materials, especially metal oxides, are widely applied in gas and humidity sensors [8] and remain the focus of much research [9,10]. A good sensing material needs to show high sensitivity, good selectivity, and be low-cost, reliable and easy to fabricate [8]. The rapid development of flexible electronics increases the need for developing sensing materials suited for such applications [11,12], such as metal oxide capacitive humidity sensors on paper [2]. Recent research has focused on developing a self-powered, flexible humidity sensor [13]. Miniaturized flexible temperature monitoring using negative temperature coefficient (NTC) materials, such as NiO, has also been a subject of research [14]. In human health monitoring, besides temperature [15],

respiration monitoring can be performed by impedance-type humidity sensors [16]. A combined multifunctional spinel ceramic humidity and temperature sensing potential was investigated by Vakiv et al. [17].

Nickel manganite is a well-known NTC thermistor oxide material, low-cost, non-toxic and abundant [18], with a cubic spinel structure and a small polaron hopping conduction mechanism between manganese cations (Mn^{3+} and Mn^{4+}) [19,20]. It has extensively been investigated as an NTC thermistor in bulk, thick or thin film form [19,21–23]. Recently, nickel manganite has been the subject of much research for energy storage as a supercapacitor, [24,25] in photocatalysis [26], or as anode material for lithium-ion batteries [27]. Gawli et al. investigated the possible application of $NiMn_2O_4$ as a humidity sensing material [28]. The structure and morphology of $NiMn_2O_4$ as a result of the synthesis method have a noticeable influence on electrical properties [23]. Different methods have been used to synthesize $NiMn_2O_4$ nanoparticles, such as sol–gel [25], solution combustion [20,27,29] and hydrothermal methods, [30] resulting in different particle morphology and properties. High surface area, mesoporous and aligned $NiMn_2O_4$ nanofibers were obtained by Bhagwan et al. [31] using electrospinning that showed improved energy storage properties.

Mesoporous metal oxides are widely applied as gas sensing materials, including humidity sensing [32]. A large surface area provides more active sites for adsorption of water molecules on the surface of the sensing material, while the porosity, derived from the right system of pores, allows better exposure to available active sites, facilitates the adsorption of H_2O in the response phase of sensor use and does not hinder the desorption of H_2O molecules in the recovery phase [33]. According to Wang et al. [34], an increase in reaction sites due to a high specific surface area of the sensing material can enhance the gas sensor activity and sensitivity. A highly porous structure with a well-connected system of transport channels suitable for fast diffusion of gas molecules results in highly sensitive sensors with a fast response and recovery [32]. Optimization of the pore structure in gas sensing materials can also result in improved selectivity [34].

In this work, we used electrospinning to obtain $NiMn_2O_4$ nanocrystalline fibers with a high specific surface area and mesoporous structure with potential as a multifunctional material, investigated here for humidity and temperature sensing.

2. Materials and Methods

2.1. Materials

Nickel nitrate hexahydrate ($Ni(NO_3)_2{\cdot}6H_2O$, purum p.a., purity $\geq$ 97%), manganese acetate tetrahydrate ($(CH_3COO)_2Mn{\cdot}4H_2O$, ACS reagent, purity $\geq$ 99%), N,N-Dimethylformamide (DMF, puriss, ACS reagent, $\geq$99.8%), absolute ethanol (ACS reagent), polyvinylpyrrolidone (PVP, M_w = 1,300,000) and deionized water were purchased from Merck (Sigma Aldrich, Darmstadt, Germany) and used as received.

2.2. Electrospinning

Nickel nitrate hexahydrate and manganese acetate tetrahydrate in the molar ratio of 1:2 were dissolved in distilled water and mixed with 5 mL of DMF dissolved in 5 mL of ethanol. The solution was mixed on a magnetic stirrer until all components were completely dissolved. PVP was slowly added to make a 10% polymer solution that was left to mix overnight. The mixture was loaded into a plastic syringe with a 0.8 mm diameter needle connected to a high voltage supply in an "in-house" designed electrospinning system. The applied voltage was maintained at 21.5 kV, while the rotating drum collector speed was 1200 rpm. The distance between the tip of the needle and the rotating drum collector was set at 12 cm, while the solution was pumped from the syringe at 1.5 mL/h. The fibers were collected on baking paper mounted on the rotating drum collector. As-spun fibers (as shown in Figure 1a) were peeled off from the paper and calcined in a chamber furnace in air at 400 °C for 4 h with a slow heating rate of 1°/min, in accordance with the literature [31].

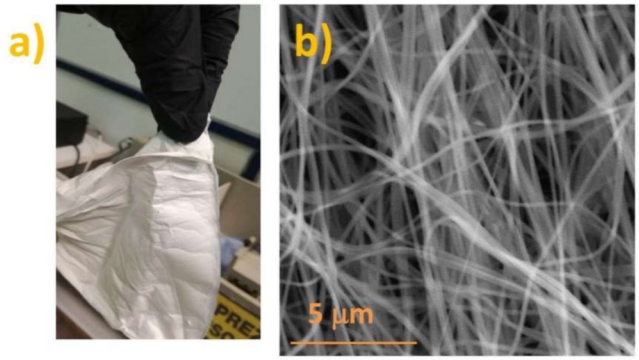

Figure 1. Photo (**a**) and SEM image (**b**) of as-spun fiber peeled off the baking paper.

2.3. Characterization of As-Spun Fibers

Simultaneous TG/DTA analysis of as-spun fibers was performed on a SETSYS Evolution 24,000 Setaram Instrumentation device (Cailure, France) up to 1000 °C with a heating rate of 5°/min in air. FT-IR spectroscopy of the as-spun fibers was performed on a FT-IR Nicolet 6700 ATR device (Thermo Fisher, UK) with the resolution of 4 cm^{-1}, in the 400–4000 cm^{-1} range. The as-spun fiber morphology was observed by scanning electron microscopy (SEM) on a TESCAN Electron Microscope VEGA TS 5130MM (Czech Republic).

2.4. Characterization of $NiMn_2O_4$ Nanocrystalline Fibers

The crystal structure of $NiMn_2O_4$ nanofibers was analyzed using X-ray diffraction (Rigaku Ultima IV diffractometer, Japan) in the 10–90° range. Functional groups were determined by FT-IR spectroscopy (on the same instrument and conditions as above). The fiber morphology was observed by field emission scanning electron microscopy (FESEM) on a TESCAN MIRA3 XM (Czech Republic). The nitrogen adsorption–desorption isotherm was collected on a Sorptomatic 1990 Thermo Finigen (Thermo Fisher, UK) at 77 K. Samples for measurement were prepared by degassing in a vacuum at 110 °C for 36 h.

2.5. Humidity and Temperature Sensing

$NiMn_2O_4$ nanocrystalline fiber powder was ground for a short time with an agate mortar and pestle, mixed with a small amount of deionized water to prepare a paste that was drop cast onto alumina substrate with small test interdigitated PdAg electrodes (finger width 0.6 mm, finger spacing 0.3 mm), previously prepared by screen printing PdAg paste onto alumina substrate combined with firing in a conveyor furnace at 850 °C for 15 min, as shown in detail in [35]. The thick film samples were dried and left to age at room temperature for several days. Change in impedance with relative humidity (RH 40–90%) was measured on a HIOKI 3532-50 LCR HiTESTER in the 42 Hz − 1 MHz frequency range and the set voltage of 1 V in a JEIO TECH TH-KE-025 temperature and humidity climatic chamber. Two operating temperatures were selected, 25 and 50 °C. The desired temperature and humidity values were obtained by initially setting the temperature and starting humidity (RH 90%). Stable temperature and humidity was established for on average 30–45 min in the temperature and humidity climatic chamber. Then, the sample was measured and a new humidity value was set, while the temperature was maintained at a constant value. When the set RH and temperature stabilized, the impedance was measured and another RH value was set. DC resistance was measured on a Tektronix DMM4040 6-1/2 digit precision multimeter in the same temperature and humidity climatic chamber while maintaining constant humidity, with RH set at 40% in the temperature interval 20–50 °C. The desired humidity and temperature values were obtained by setting RH at 40% and the initial temperature at 20 °C. When this was established (after 30–45 min) the resistance was measured, and another temperature value was set, while the RH was constant. When the set temperature value stabilized, the sensor resistance was measured again.

3. Results and Discussion

3.1. As-Spun Fibers

As-spun fibers were smooth and randomly oriented with a uniform surface (Figure 1). The mean fiber diameter was determined by measurement of the width of 40 nanofibers in recorded SEM images using the Gatan Micrograph® software as 238 nm with values ranging from 130 to 430 nm.

The FT-IR spectrum of as-spun fiber (Figure 2a) shows bands originating from PVP, DMF, nickel nitrate and manganese acetate precursors. OH group vibrations in the 3000–3500 cm^{-1} range are noted, belonging to residual water in the fibers [36–38]. The bending vibration of the OH group, usually noted around 1635 cm^{-1} [38] is possibly present but masked by the C=O stretching vibration noted at ≈1650 cm^{-1} of the carbonyl group in PVP [39]. C−H stretching, and bending vibrations of the CH_2 group in PVP were noted at ≈2959 cm^{-1} and 1420 cm^{-1}, respectively [37,39]. Tertiary amine C−N stretching vibrations can be noted at ≈1290 cm^{-1} [40], while absorption of the C−N vibration of PVP can be noted at ≈1021 cm^{-1} [37]. CH_2 rocking vibrations of PVP can be noted at ≈845 cm^{-1} [39]. The bands in the range of 1580 to 1560 cm^{-1} and ≈1462 cm^{-1} can be assigned to asymmetric and symmetric vibrations of C−O originating from the acetate ion in the manganese acetate precursor [41]. Vibrations of nitrate groups in the nickel nitrate precursor expected at 1620 and 1380 cm^{-1} are masked by the C=O stretching vibration and C−H bending vibrations of PVP, respectively [42]. A small vibration band at 826 cm^{-1} can be attributed to the bending mode of the nitrate group [37], while the vibration band at 653 cm^{-1} can be due to both the vibrational mode of nitrate groups in the nickel nitrate precursor, and Mn−O vibration in the manganese acetate precursor [37,41].

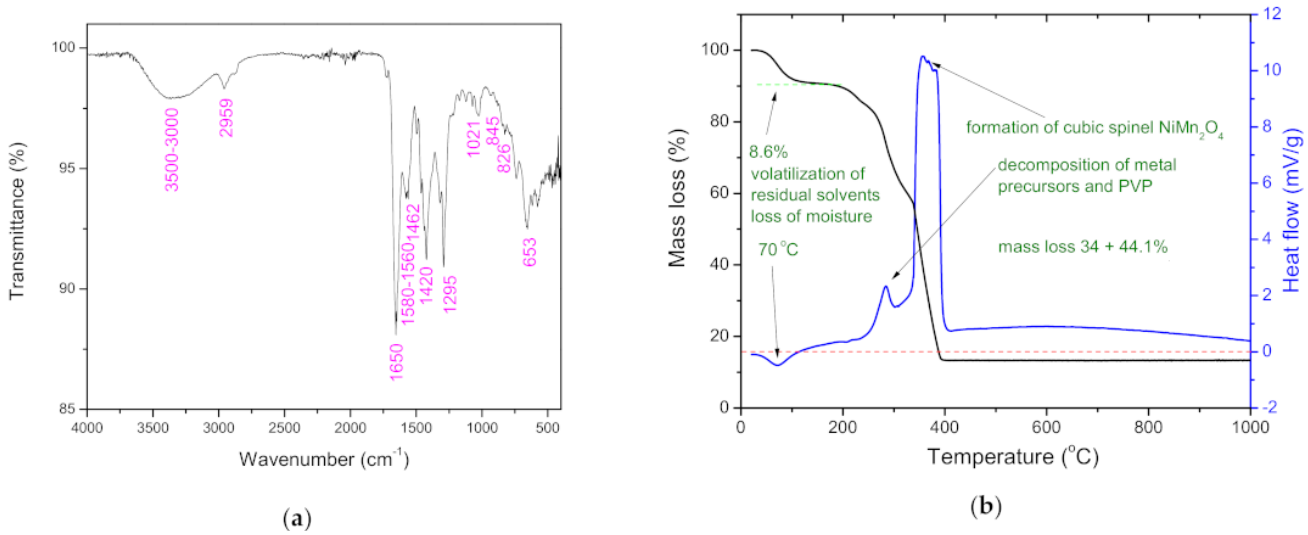

Figure 2. FT-IR spectrum (**a**) and TG/DTA plots (**b**) measured on as-spun fibers.

The measured TG/DTA in Figure 2b shows the thermal behavior of the as-spun fibers. The total mass loss was ≈86.7% up to 400 °C, after which it remained constant in the temperature region 400–1000 °C. The mass loss can be divided into three regions in accordance with Bhagwan et al. [31] who determined the same for electrospun nickel manganite fibers. It started with volatilization of the residual solvents present in fibers (DMF, ethanol) and loss of moisture/desorption of water (H_2O) [36] corresponding to the initial minor mass loss of ≈8.6% from ≈20 to 113 °C, and endothermic peak at ≈70 °C. A small exothermic peak at ≈284 °C, followed by a distinct wide exothermic peak with a maximum at ≈357 °C can be noted, accompanied by a weight loss of 34 and 44.1%, respectively. Both peaks may be ascribed to decomposition of the metal precursors and PVP in the electrospun fibers, but the second can be ascribed to complete decomposition and removal of PVP and formation of the cubic spinel structure [31,37].

3.2. $NiMn_2O_4$ Nanofibers

Calcination of the as-spun fibers resulted in the formation of $NiMn_2O_4$ nanocrystalline fibers. The characteristic reflections on the measured X-ray diffraction pattern (Figure 3a) could be assigned to the $Fd\bar{3}m$ cubic spinel structure, in accordance with the ICCD/JCPDS card 71-0852 [43]. The measured FT-IR spectrum (Figure 3b) showed that all organics from PVP have burnt out, leaving only a small incline at ≈3385 cm^{-1} and ≈1641 cm^{-1} from OH group stretching and bending bands due to readsorbed atmospheric H_2O in the $NiMn_2O_4$ spun fibers. This was noted before for electrospun $NiFe_2O_4$ fibers [37]. The noticeable bands at ≈575, 414 and the small incline at ≈490 cm^{-1} can be attributed to vibration bands originating from tetrahedral and octahedral groups of $Mn^{3+}-O$, $Ni^{2+}-O$ [43,44] and, according to Bhagwan et al. [31], also $Ni-O-Mn$ vibrations in $NiMn_2O_4$, confirming the formation of $NiMn_2O_4$ after calcination.

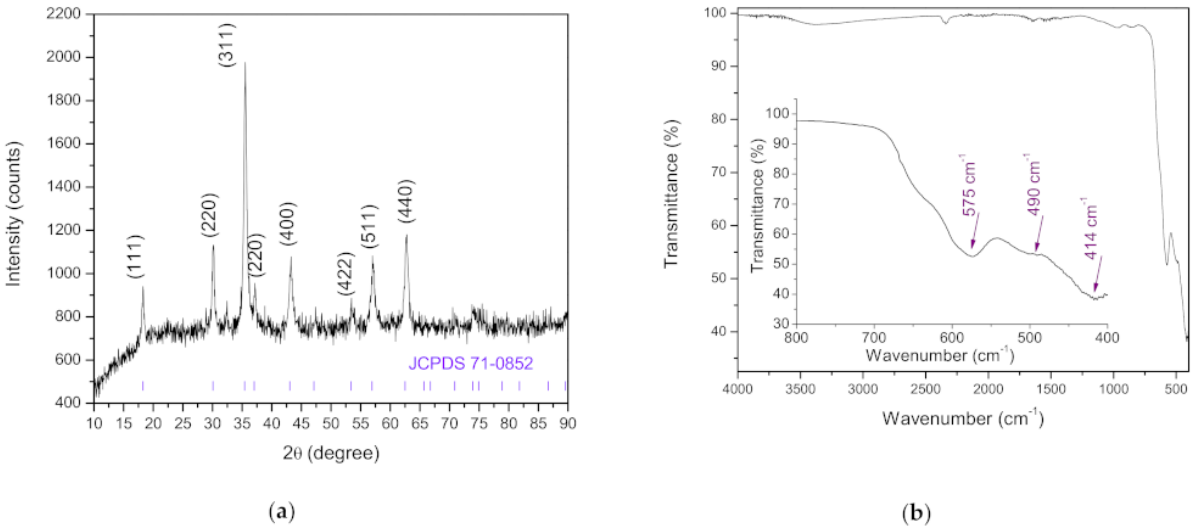

Figure 3. XRD diffractogram (**a**) and FT-IR spectrum (**b**) measured on $NiMn_2O_4$ nanocrystalline fibers.

The morphology of $NiMn_2O_4$ nanofibers is shown in Figure 4a. The fiber network structure remained after calcination. The fiber width decreased due to removal of the polymer component (PVP backbone) and crystallization of the metal component, as shown before in the literature [31,45–47]. The average fiber diameter was 207 nm, with values ranging from 160 to 250 nm. The fibers are composed of small interconnected $NiMn_2O_4$ nanoparticles (as shown in the inset in Figure 4a) in the range of 20 to 50 nm, similar to the morphology obtained by Bhagwan et al. [31].

The measured nitrogen adsorption–desorption isotherm (Figure 4b) is of type II, according to the IUPAC nomenclature [48]. However, the obvious presence of hysteresis of the loop, in the region of relative pressure (p/p_0) higher than 0.8, reveals the presence of high diameter mesopores, as well. The pore size distribution curve is given as an inset in Figure 4b and shows pores ranging from 2 to 63 nm including macropores > 50 nm besides mesopores (2–50 nm). Indeed, the value of mesopore volume (0.089 cm^3/g), determined by the BJH method, represents 52% of the total pore volume determined by the Gurevich method for $p/p_0 = 0.99$. Additionally, the most significant contribution to the total specific surface area of 25.3 m^2/g, calculated using the Brunauer–Emmett–Teller (BET) equation, originates from the mesopores' specific surface area of 21.5 m^2/g (calculated with the BJH method). In contrast, the volume of micropores determined by the t-plot method is small; 0.005 cm^3/g. Overall, similar to Bhagwan et al. [31], we obtained high surface area mesoporous $NiMn_2O_4$ nanocrystalline fibers.

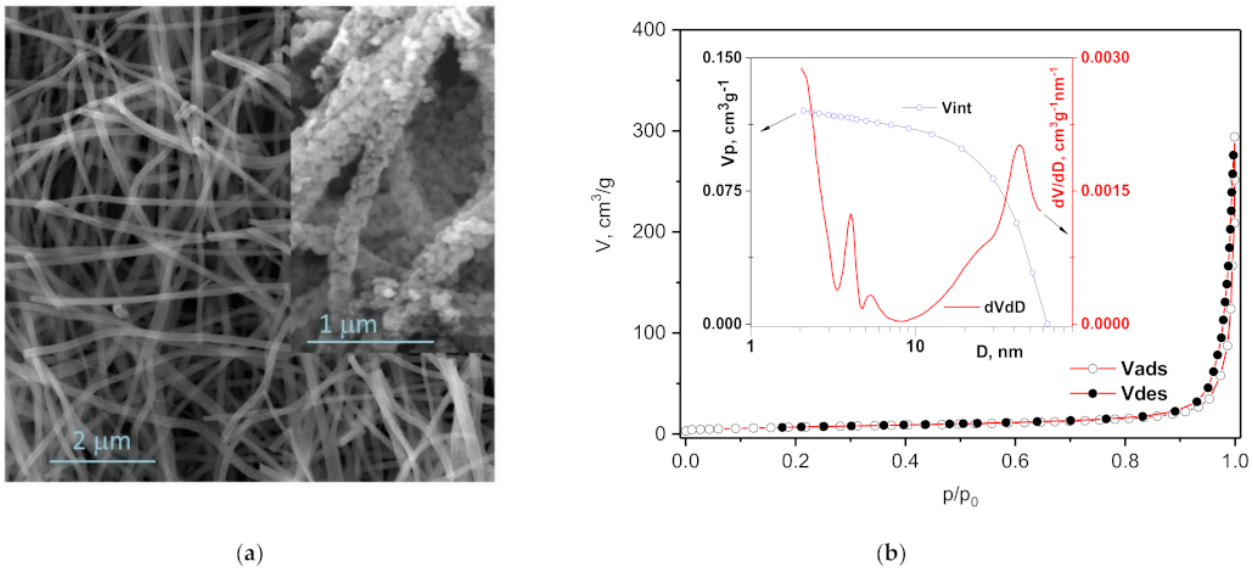

Figure 4. FESEM images (**a**) and nitrogen adsorption–desorption isotherms (**b**) of $NiMn_2O_4$ nanocrystalline fibers inset: pore size distribution.

3.3. NTC Temperature Dependence of DC Resistance

As noted before for $NiMn_2O_4$ [18,19,29] as an NTC thermistor material, the measured DC resistance decreased with an increase in temperature (20–50 °C), following an exponential Arrhenius dependence [18], as shown in Figure 5 and the equation

$$R_T = R_\infty e^{B/T} \quad (1)$$

where R_∞ is the reference resistance of the thermistor, representing resistance at an infinite temperature when $1/T = 0$, T is the temperature expressed in K, and B is the material constant (or B-value) of the thermistor.

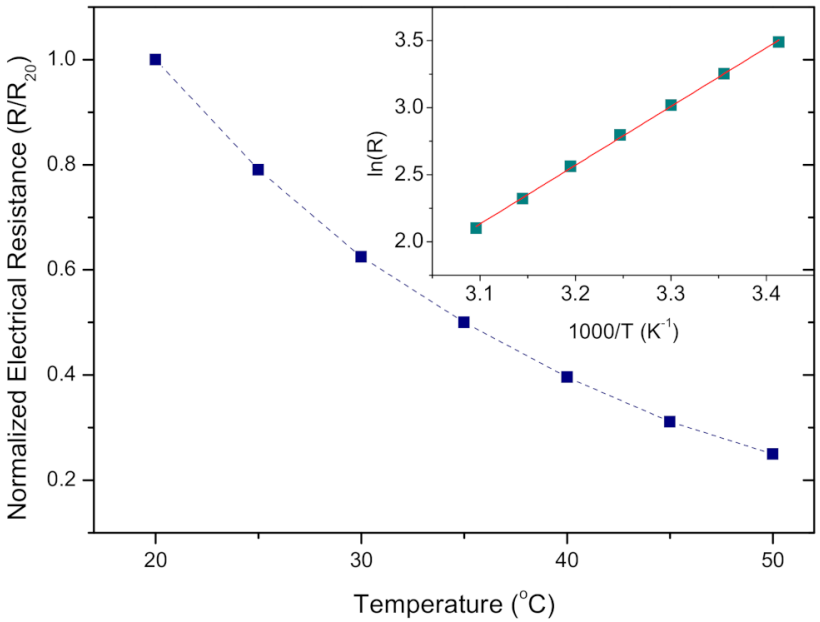

Figure 5. Electrical resistance of $NiMn_2O_4$ nanocrystalline fibers; inset represents an estimation of the material constant (B).

In our case, the change in resistance was monitored in a temperature and humidity climatic chamber, maintaining a constant relative humidity (RH) of 40% (the most common value of RH in our laboratory and surrounding environment) and changing the temperature, as the change in RH had an influence on overall resistance values.

The material constant (B) of the thermistor (B-value) was estimated from the linear fit (as shown in the inset in Figure 5) as 4397 K in the temperature interval 20–50 °C. This value is within the range used in commercial NTC bulk ceramics (2000–5000 K) [18,49], slightly lower than the value of 4812 K determined for $NiMn_2O_4$ powder obtained by sol–gel combustion [29], lower than for $LaNiO_3$-$NiMn_2O_4$ nanocomposite thick films [50] where B was over 5000 K, or the significantly high B value of 7350 K obtained for NiO temperature sensors by Shin et al. [15], all obtained at room temperature. Wang et al. obtained the B-value of 4310 K for miniature nickel oxide thick film thermistors printed using aerosol jet technology [51]. Schubert et al. [52] obtained the B-value of 4250 for aerosol as-deposited films, that decreased to the 3500–3900 K range with film firing in the temperature interval of 200 to 600 °C. Bulk nickel manganite NTC thermistors most often have B-values in the 3500–3900 K range, as recently determined by Li et al. [53] for a core–shell NTC ceramic, or 3500 K determined by Reiman et al. [54] for a multilayer Ni-Zn-Co-Mn-O NTC ceramic fired at 900 °C.

The temperature sensitivity at room temperature (25 °C) was determined as $\alpha = -4.95\%/\mathrm{K} = 1/R \cdot \mathrm{d}R/\mathrm{d}T = -B/T^2$. This value is comparable with commercial devices (−4%/K) [18,49] and confirms the potential of application of $NiMn_2O_4$ nanocrystalline fibers in temperature sensing, especially as these values were obtained for drop-cast powder with no further temperature treatment. $NiMn_2O_4$ nanocrystalline fibers could be applied in temperature sensors in the form of ink on flexible substrates that can tolerate only low-temperature treatment of the sensing layer [15].

3.4. Influence of Humidity on Complex Impedance

At both operating temperatures (25 and 50 °C), the measured impedance decreased with the increase in relative humidity (RH), and also with the change in frequency, as shown in Figure 6a for the operating temperature of 25 °C. The complex impedance magnitude becomes smaller with an increase in RH, as shown in Figure 6b.

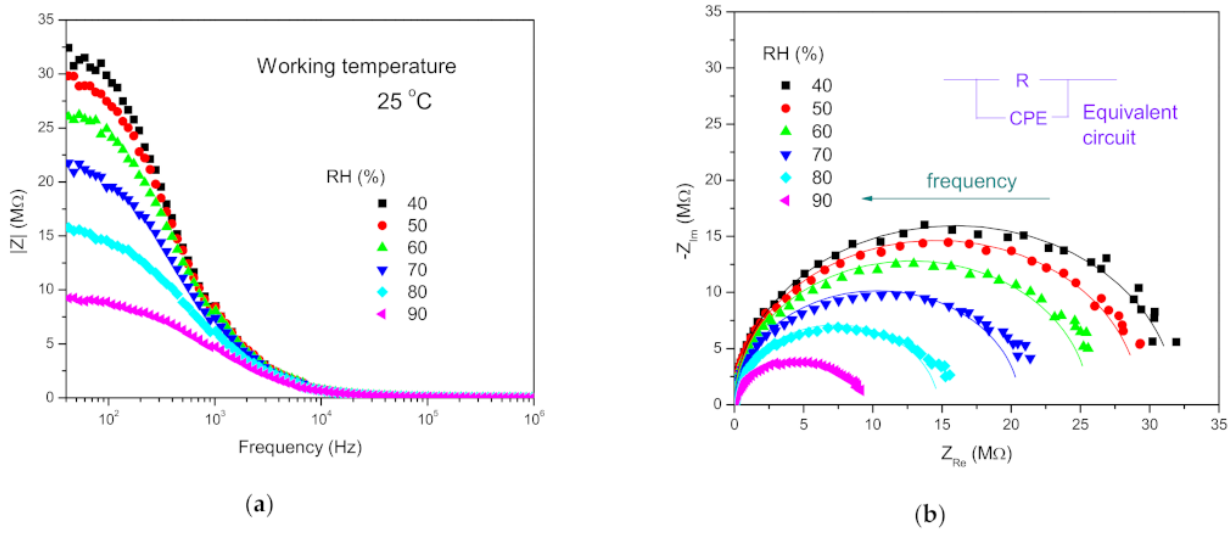

Figure 6. Impedance dependence on frequency (**a**) and complex impedance (**b**) measured (points) and fitted (line) using the equivalent circuit shown in the inset, for relative humidity RH 40-90% of $NiMn_2O_4$ nanocrystalline fibers at the working temperature of 25 °C.

One dielectric relaxation process was noted for complex impedance. This has been noted before for metal oxide semiconductors, including nickel manganite [20,28,55,56].

Highly conducting grains and the resistive nature of grain boundaries present in nickel manganite contribute to this relaxation process [57]. One semicircle shows that either one relaxation process (originating from grains or grain boundaries) is dominant, or grain and grain boundary contributions overlap [58,59]. Adsorption of water molecules by a surface reaction mechanism with the nanocrystalline fiber particles of $NiMn_2O_4$ with a rise in RH leads to an increase in ionic conductivity in accordance with the humidity sensing mechanism [35,60]. This was most noticeable in the lower frequency range, as shown in Figure 7 for several selected frequencies.

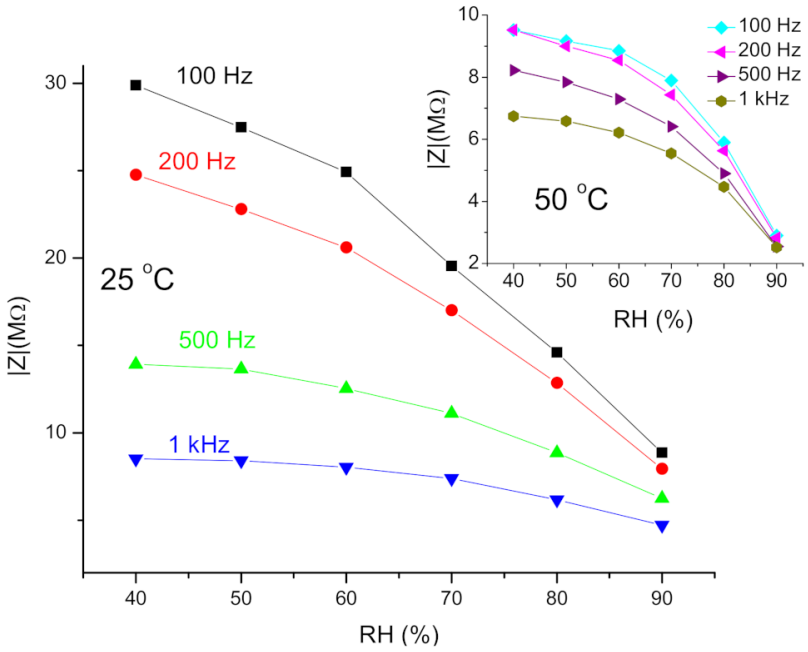

Figure 7. Impedance dependence on RH measured at selected frequencies.

The sensitivity, defined as the ratio between the change of sensor impedance and RH ($\Delta Z/\Delta RH$) at 100 Hz, was determined as 327.36 ± 80.12 kΩ/%RH at 25 °C. It decreased with an increase in frequency, and was 259.33 kΩ/%RH, 93.34 kΩ/%RH, 40.71 kΩ/RH at 200, 500 and 1000 Hz, respectively. At the working temperature of 50 °C, the sensitivity at 100 Hz was determined as 69.88 kΩ/%RH. A similar decrease in sensitivity with frequency was noted by Zhang et al. [60]. The obtained sensitivity value at 100 Hz of 327.36 kΩ/%RH is comparable with sensitivity data determined for NiO/SnO_2 electrospun fibers [61] and nanocrystalline Zn_2SnO_4/SnO_2 composite [35], confirming the potential of $NiMn_2O_4$ nanocrystalline fibers for application in humidity sensing.

The measured complex impedance spectra (as shown in Figure 6b at the working temperature of 25 °C) were analyzed using an equivalent circuit consisting of a parallel resistance and constant phase element (CPE), as it was not possible to separate the influence of grain and grain boundary components of the measured impedance, as shown in the inset in Figure 6b. The CPE element was used, as we expected non-ideal Debye capacitance behavior previously noted for $NiMn_2O_4$ synthesized by refluxing nickel oleate and manganese oleate [28], and other metal oxides, such as $FeMnO_3$ [55] or Fe_2TiO_5 [56]. Fitting of experimental data to the proposed equivalent circuit was performed using the EIS Spectrum Analyzer Software [62]. Good agreement was obtained between measured and fitted data, as shown in Figure 6b. The small deviation at low frequencies for high humidity can be attributed to a combined grain boundary and electrode effect. The obtained values determined for resistance, capacitance and the critical exponent (n) are shown in Table 1.

Table 1. Resistance, capacitance and critical exponent calculated from measured complex impedance spectra using the equivalent circuit composed of a parallel resistance and CPE element.

Working Temperature 25 °C				
Relative Humidity (%)	**R (MΩ)**	**C (pF)**	**n**	**f_{rel} (Hz)**
40	31.898	20.151	1	1555
50	29.272	20.142	1	1696
60	25.693	20.542	0.99807	1894
70	20.644	21.903	0.98948	2211
80	14.750	24.264	0.97599	2794
90	8.823	27.206	0.96038	4262
Working Temperature 50 °C				
Relative Humidity (%)	**R (MΩ)**	**C (pF)**	**n**	**f_{rel} (Hz)**
40	9.727	19.852	1	5178
50	9.479	19.972	1	5282
60	8.768	20.293	0.99868	5622
70	7.643	21.126	0.99234	6192
80	5.715	22.577	0.98297	7749
90	2.806	29.096	0.95068	12,245

The capacitance was calculated taking into account the case of parallel resistance and CPE element, as described in detail in [58]. The determined capacitance increased slightly with an increase in RH in a similar range for both working temperatures. Its value was between 19.8 and 29.1 pF, indicating the dominant influence of grains, as grain capacitance values fall in this range, as noted previously for $NiMn_2O_4$ powder obtained by sol-gel auto-combustion [20], or $Ni_{0.54}Mn_{1.26}Fe_{1.2}O_4$ NTC ceramic thermistors obtained by spark plasma sintering [59]. In the case of electrospun $NiMn_2O_4$ nanocrystalline fibers, at low relative humidity values (RH 40, 50%) at both working temperatures, the dependence of complex impedance on frequency represented an ideal semicircle (the critical exponent n was one). As the relative humidity increased the n value decreased, though it remained relatively close to 1, reaching 0.96038 and 0.95068 for RH 90% at the working temperatures of 25 and 50 °C, respectively. This shows that the behavior of $NiMn_2O_4$ nanocrystalline fibers was close to perfect Debye, with the measured complex impedance semicircle showing only a slight depression that increased with an increase in RH from 60 to 90%. Similar values of the critical exponent (between 0.97 and 1) were noted before for $NiMn_2O_4$ thin films, but for the change in temperature in the 180–500 K range [63].

The dielectric relaxation frequency was determined as $2\pi f_{rel} = 1/R{\cdot}C$ and it shifted towards higher values with an increase in RH, and also with working temperature (as shown in Table 1). The determined resistance decreased noticeably with the increase in RH similar to the impedance decrease, reflecting the water adsorption (humidity sensing) mechanism (shown in Figure 8) by $NiMn_2O_4$ nanocrystalline fibers.

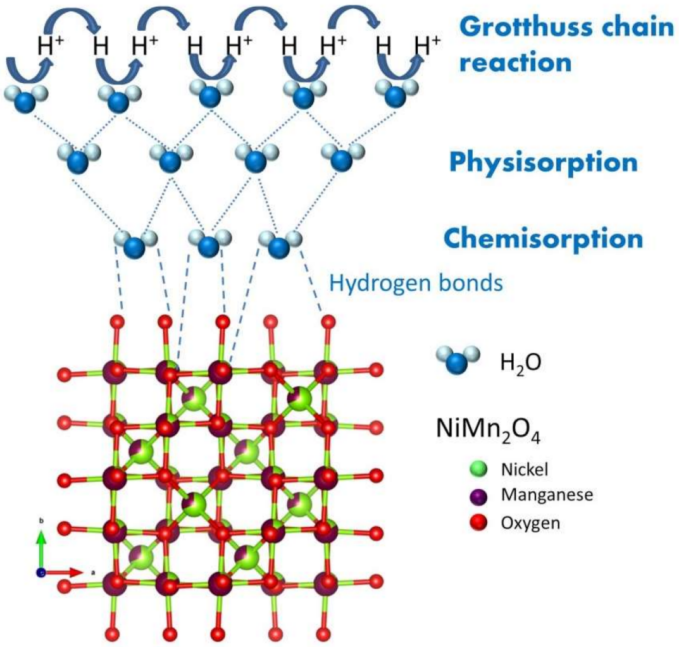

Figure 8. Humidity sensing mechanism of nickel manganite nanocrystalline fibers, $NiMn_2O_4$ $Fd\bar{3}m$ cubic spinel structure drawn using VESTA [64].

At low RH, water molecules are chemisorbed by the mesoporous nanocrystalline $NiMn_2O_4$ fibers on the sample surface. Hydrogen bonds form firmly attached OH groups. With the increase in RH, more water molecules are physically adsorbed on the chemisorbed layer. High RH leads to the formation of multiple physisorbed layers. Mobility of water molecules is enabled by single hydrogen bonding with H^+ acting as the dominant charge carrier. A Grotthuss chain reaction (charge transport mechanism) is used to describe the conductivity [65]. A proton is released by H_3O^+ to a water molecule that is close by and ionized, forming H_3O^+ again. This results in proton hopping between water molecules, increased conductivity, reduced resistance, shrinking the complex impedance semicircles and a shift in the dielectric relaxation frequency towards higher values.

4. Conclusions

High surface (25.3 m^2/g) mesoporous nanocrystalline nickel manganite fibers with a cubic spinel structure were obtained using the electrospinning method, followed by calcination at 400 °C with a slow heating rate of 1°/min. Drop-casting a paste made from the obtained powder and water on test interdigitated alumina electrodes enabled determination of the B constant as 4379 K in the 20–50 °C temperature range, and a temperature sensitivity of −4.95%/K at 25 °C. The sensitivity of 327.36 kΩ/%RH in the relative humidity range of 40 to 90% confirmed the potential of electrospun nanocrystalline $NiMn_2O_4$ fibers as a multifunctional material for combined temperature and humidity sensing.

Author Contributions: M.V.N. conceived the study, measured and analyzed FT-IR spectra, measured and analyzed DC resistance and AC impedance; M.P.D. and Z.Z.V. designed and performed material synthesis, measured DC resistance and AC impedance; J.B.K. measured and analyzed N_2 physisorption at 77 K; J.D.V. measured and analyzed FESEM images; S.M. measured and analyzed TG/DTA; N.B.T. performed XRD characterization; writing—original draft preparation, J.B.K. and M.V.N.; writing—review and editing, M.P.D., Z.Z.V. and S.M. All authors have read and agreed to the published version of the manuscript.

Funding: This research was funded by the Ministry for Education, Science and Technology Development under the contact 451-03-9/2021-14/200053 (MPD, ZZV, MVN); 451-03-9/2021-14/200026 (JBK) 451-03-9/2021-14/200175 (JDV, SM).

Institutional Review Board Statement: Not applicable.

Informed Consent Statement: Not applicable.

Data Availability Statement: The data presented in this study are available on request from the corresponding author. The data are not publicly available due to ongoing research.

Acknowledgments: J.D.V. measured the FESEM images at the Faculty of Technology and Metallurgy, University of Belgrade.

Conflicts of Interest: The authors declare no conflict of interest. The funders had no role in the design of the study, in the collection, analyses, or interpretation of data, in the writing of the manuscript, or in the decision to publish the results.

References

1. Faharani, H.; Wagiran, R.; Hamidon, N.M. Humidity sensors principle, mechanism and fabrication technologies: A comprehensive review. *Sensors* **2014**, *14*, 7881–7939. [CrossRef] [PubMed]
2. McGhee, J.R.; Sagu, J.S.; Southee, D.J.; Evans, P.S.A.; Wijayantha, K.G.U. Printed, fully metal oxide, capacitive humidity sensors using conductive indium tin oxide inks. *ACS Appl. Electron. Mater.* **2020**, *2*, 3593–3600. [CrossRef]
3. Firouz, M.S.; Mohi-Alden, K.; Omid, M. A critical review on intelligent and active packaging in the food industry: Research and development. *Food Res. Inter.* **2021**, *141*, 110113. [CrossRef] [PubMed]
4. Imam, S.A.; Choudhary, A.; Sachan, V.K. Design issues for wireless networks and smart humidity sensors for precision agriculture: A review. In Proceedings of the 2015 International Conference on Soft Computing Techniques and Implementations (ICSCTI), Faridabad, India, 8–10 October 2015; pp. 181–187. [CrossRef]
5. Goel, K.; Bindal, A.K. Wireless sensor network in precision agriculture: A survey report. In Proceedings of the 2018 Fifth International Conference on Parallel, Distributed and Grid Computing (PDGC), Solan, India, 20–22 December 2018; pp. 176–181. [CrossRef]
6. Ezhilazhahi, A.M.; Bhuraneswari, P.T.V. IoT enabled plant soil moisture monitoring using wireless sensor networks. In Proceedings of the 2017 Third International Conference on Sensing, Signal Processing and Security (ICSSS), Chennai, India, 4–5 May 2017; pp. 345–349. [CrossRef]
7. Tulliani, J.M.; Baroni, C.; Zavattaro, L.; Grignani, C. Strontium-doped hematite as possible humidity sensing material for soil water content determination. *Sensors* **2013**, *13*, 12070–12092. [CrossRef]
8. Nikolic, M.V.; Milovanovic, V.; Vasiljevic, Z.Z.; Stamenkovic, Z. Semiconductor gas sensors: Materials, technology, design and application. *Sensors* **2020**, *20*, 6694. [CrossRef]
9. Shakeen, K.; Shah, Z.; Khan, B.; Adnan; Omer, M.; Alamzeb, M.; Suo, H. Electrical, photocatalytic and humidity sensing application of mixed metal oxide nanocomposites. *ACS Omega* **2020**, *5*, 7271–7279. [CrossRef]
10. Tripathy, A.; Pramanik, S.; Cho, J.; Santosh, J.; Osman, N.A.A. Role of morphological structure, doping and coating of different materials in the sensing characteristics of humidity sensors. *Sensors* **2014**, *14*, 1643–16422. [CrossRef]
11. Zhang, D.; Zong, X.; Wu, Z.; Zhang, Y. Hierarchical self-assembled SnS_2 nanoflower Zn_2SnO_4 hollow sphere nanohybrid for humidity sensing applications. *ACS Appl. Mater. Interfaces* **2018**, *10*, 32631–32639. [CrossRef]
12. Baldo, T.A.; de Lima, L.F.; Mendes, L.F.; de Aranjo, W.R.; Paixao, T.R.L.C.; Coltro, W.K.T. Wearable and biodegradable sensors for clinical and environmental applications. *ACS Appl. Electron. Mater.* **2021**, *3*, 68–100. [CrossRef]
13. Faharani, E.; Mohammadpour, R. Fabrication of flexible self-powered humidity sensor based on super-hydrophilic titanium oxide nanotube arrays. *Sci. Rep.* **2020**, *10*, 13032. [CrossRef]
14. Huang, C.C.; Kao, Z.K.; Liao, Y.C. Flexible miniaturized nickel oxide thermistor arrays via inkjet printing technology. *ACS Appl. Mater. Interfaces* **2013**, *5*, 12954–12959. [CrossRef]
15. Shin, J.; Jeong, B.; Kim, J.; Nam, V.B.; Yoon, Y.; Jung, J.; Hong, S.; Lee, H.; Eom, H.; Yeo, J.; et al. Sensitive Wearable Temperature Sensor with Seamless Monolithic Integration. *Adv. Mater.* **2019**, *32*, e1905527. [CrossRef]
16. Wu, Z.; Yang, J.; Sun, X.; Wu, Y.; Wang, L.; Meng, G.; Kuang, D.; Guo, X.; Qu, W.; Du, B.; et al. An excellent impedance-type humidity sensor based on halide perovskite CsPbBr3 nanoparticles for human respiration monitoring. *Sensors Actuators B Chem.* **2021**, *337*, 129772. [CrossRef]
17. Vakiv, M.; Hadzaman, I.; Klym, H.; Shpotyuk, O.; Bruner, M. Multifunctional thick-film structures based on spinel ceramics for environmental sensors. *J. Phys. Conf. Ser.* **2011**, *289*, 012011. [CrossRef]
18. Feteira, A. Negative temperature coefficient resistance (NTCR) ceramic thermistors: An industrial perspective. *J. Am. Ceram. Soc.* **2009**, *92*, 967–983. [CrossRef]
19. Schubert, M.; Münch, C.; Schuurman, S.; Poulain, V.; Kita, J.; Moos, R. Novel Method for NTC Thermistor Production by Aerosol Co-Deposition and Combined Sintering. *Sensors* **2019**, *19*, 1632. [CrossRef] [PubMed]
20. Karmarkar, S.; Behera, D. Small polaron hopping conduction in $NiMnO_3/NiMn_2O_4$ nano-cotton and its emerging energy application with MWCNT. *Ceram. Int.* **2019**, *45*, 13052–13066. [CrossRef]
21. Gao, H.; Ma, C.; Sun, B. Preparation and characterization of $NiMn_2O_4$ negative temperature ceramics by solid-state coordination reaction. *J. Mater. Sci. Mater. Electron.* **2014**, *25*, 3990–3995. [CrossRef]

22. Ryu, J.; Kim, K.-Y.; Choi, J.-J.; Hahn, B.-D.; Yoon, W.-H.; Lee, B.-K.; Park, D.-S.; Park, C. Highly Dense and Nanograined NiMn2O4Negative Temperature coefficient Thermistor Thick Films Fabricated by Aerosol-Deposition. *J. Am. Ceram. Soc.* **2009**, *92*, 3084–3087. [CrossRef]
23. Fritsch, S.; Sarrias, J.; Brien, M.; Conderc, J.J.; Bandour, J.L.; Snoeck, E.; Rousset, A. Correlation between the structure, the microstructure and the electrical properties of nickel manganite negative temperature coefficient (NTC) thermistors. *Solid State Ion.* **1998**, *109*, 229–237. [CrossRef]
24. Sun, Y.; Zhang, J.; Sun, X.; Huang, N. High-performance spinel $NiMn_2O_4$ microspheres self-assembled with nanosheets by microwave-assisted synthesis for supercapacitor. *CrystEngComm.* **2020**, *22*, 1645–1652. [CrossRef]
25. Ray, A.; Roy, A.; Ghosh, M.; Ramos-Ramon, J.A.; Saha, S.; Pal, U.; Bhattarcharya, S.K.; Das, S. Study on charge storage mechanism in working electrodes fabricated by sol-gel derived spinel $NiMn_2O_4$ nanoparticles for supercapacitor application. *Appl. Surf. Sci.* **2019**, *463*, 513–525. [CrossRef]
26. Larbi, T.; Doll, K.; Amlouk, M. Temperature dependence of Raman spectra and first principles study of NiMn2O4 magnetic spinel oxide thin films. Application in efficient photocatalytic removal of RhB and MB dyes. *Spectrochim. Acta Part A Mol. Biomol. Spectrosc.* **2019**, *216*, 117–124. [CrossRef]
27. Rajoba, S.; Kale, R.; Kulkarni, S.; Parale, V.; Patil, R.; Olin, H.; Park, H.-H.; Dhavale, R.; Phadatare, M. Synthesis and Electrochemical Performance of Mesoporous $NiMn_2O_4$ Nanoparticles as an Anode for Lithium-Ion Battery. *J. Compos. Sci.* **2021**, *5*, 69. [CrossRef]
28. Gawli, Y.; Badadhe, S.; Basu, A.; Guin, D.; Shelke, M.V.; Ogale, S. Evaluation of n-type ternary metal oxide $NiMn_2O_4$ nanomaterial for humidity sensing. *Sens. Actuators B* **2014**, *191*, 837–843. [CrossRef]
29. Nikolic, M.V.; Vasiljevic, Z.Z.; Dojcinovic, M.P.; Tadic, N.B.; Radovanovic, M.; Stojanovic, G.M. Nanocrystalline nickel manganite synthesis by sol-gel combustion for flexible temperature sensors. In Proceedings of the 2020 IEEE International Conference on Flexible and Printable Sensors and System (FLEPS), Manchester, UK, 16–19 August 2020. [CrossRef]
30. Saha, S.; Roy, A.; Ray, A.; Das, S.; Nandi, M.; Ghosh, B.; Das, S. Effect of particle morphology on the electrochemical performance of hydrothermally synthesized $NiMn_2O_4$. *Electrochim. Acta* **2020**, *353*, 136515. [CrossRef]
31. Bhagwan, J.; Rani, S.; Sivasankaran, V.; Yadav, K.L.; Sharma, Y. Improved energy storage, magnetic and electrical properties of aligned, mesoporous and high aspect ratio nanofibers of spinel $NiMn_2O_4$. *Appl. Surf. Sci.* **2017**, *426*, 913–923. [CrossRef]
32. Geng, W.; Ma, Z.; Yang, J.; Duan, L.; Li, F.; Zhang, Q. Pore size dependent acetic acid gas sensing performance of mesoporous CuO. *Sensors Actuators B Chem.* **2021**, *334*, 129639. [CrossRef]
33. Zhao, J.; Liu, Y.; Li, X.; Lu, G.; You, L.; Liang, X.; Liu, F.; Zhang, T.; Du, Y. Highly sensitive humidity sensor based on high surface area mesoporous $LaFeO_3$ prepared by nanocasting route. *Sens. Actuators B* **2013**, *181*, 802–809. [CrossRef]
34. Wang, J.; Wan, J.; Wang, D. Hollow multishelled structures for promising applications: Understanding the structure-performance correlation. *Acc. Chem. Res.* **2019**, *52*, 2169–2178. [CrossRef]
35. Nikolic, M.V.; Dojcinovic, M.P.; Vasiljevic, Z.Z.; Lukovic, M.D.; Labus, N.J. Nanocomposite Zn_2SnO_4/SnO_2 thick films as a humidity sensing material. *IEEE Sens. J.* **2020**, *20*, 7509–7516. [CrossRef]
36. Maensiri, S.; Sagmanee, M.; Wiengmoon, A. Magnesium ferrite ($MgFe_2O_4$) nanostructures fabricated by electrospinning. *Nanoscale Res. Lett.* **2009**, *4*, 221–228. [CrossRef]
37. Saensuk, O.; Phokha, S.; Bootcharnot, A.; Maensiri, S.; Swatsitang, E. Fabrication and magnetic properties of $NiFe_2O_4$ nanofibers obtained by electrospinning. *Ceram. Int.* **2015**, *41*, 8133–8141. [CrossRef]
38. Wang, Z.; Pakoulev, A.; Pang, Y.; Dlott, D.D. Vibrational substructure in the OH stretching of water and HOD. *J. Phys. Chem. A* **2004**, *108*, 9054–9063. [CrossRef]
39. Chalkias, D.A.; Giannopoulos, D.I.; Kollia, E.; Petala, A.; Kosopoulos, V.; Papanicolau, G.C. Preparation of polyvinylpyrrolidone-based polymer electrolytes and their application by in-situ gelatin in dye sensitized solar cells. *Electrochim. Acta* **2018**, *271*, 632–640. [CrossRef]
40. Vu, D.; Li, X.; Li, Z.; Wang, C. Phase-structure effects of electrospun TiO_2 nanofiber membranes on As (III) adsorption. *J. Chem. Eng. Data* **2013**, *58*, 71–77. [CrossRef]
41. Zhang, C.; Li, X.; Bian, X.; Zheng, T.; Wang, C. Polyacronitrile/manganese acetate composite nanofibers and their catalysis performance on chromium (VI) reduction by oxalic acid. *J. Hazard. Mater.* **2012**, *229–230*, 439–445. [CrossRef]
42. Naseri, M.G.; Saion, E.B.; Ahangar, H.A.; Hashim, M.; Shaari, A.H. Simple preparation and characterization of nickel ferrite nanocrystals by a thermal treatment method. *Powder Technol.* **2011**, *212*, 80–88. [CrossRef]
43. Sankar, K.V.; Surendran, S.; Pandi, K.; Allin, A.M.; Nithya, V.D.; Lee, Y.S.; Selvan, R.K. Studies on the electrochemical intercalation/de-intercalation mechanism of $NiMn_2O_4$ for high stable pseudocapacitor electrodes. *RSC Adv.* **2015**, *5*, 27649–27656. [CrossRef]
44. Savic, S.M.; Nikolic, M.V.; Paraskevopoulos, K.M.; Zorba, T.T.; Nikolic, N.; Blagojevic, V.; Aleksic, O.S.; Brankovic, G. Far infrared and microstructural studies of mechanically activated nickel manganite. *Ceram. Int.* **2013**, *39*, 1241–1247. [CrossRef]
45. Zhang, Y.; Luo, L.; Zhang, Z.; Ding, Y.; Lu, S.; Deng, D.; Zhao, H.; Chen, Y. Synthesis of $MnCo_2O_4$ nanofibers by electrospinning and calcination: Application for a highly sensitive non-enzimatic glucose sensor. *J. Mater. Chem. B* **2014**, *2*, 529–535. [CrossRef]
46. Keereeta, Y.; Thongtem, T.; Thongtem, S. Characterization of $ZnMoO_4$ nanofibers synthesized by electrospinning calcination combinations. *Mater. Lett.* **2012**, *68*, 265–268. [CrossRef]
47. Li, J.M.; Zeng, X.L.; Mo, A.D.; Xu, Z.A. Fabrication of cuprate superconducting $La_{1.85}Sr_{0.15}CuO_4$ nanofibers by electrospinning and subsequent calcination in oxygen. *CrystEngComm* **2011**, *13*, 6964–6967. [CrossRef]

48. Thommes, M.; Kaneko, K.; Neimark, A.V.; Olivier, J.P.; Rodriguez-Reinoso, F.; Rouquerol, J.; Sing, K.S.W. Physisorption of gases, with special reference to the evaluation of surface area and pore size distribution. (IUPAC Technical Report). *Pure Appl. Chem.* **2015**, *87*, 1051–1069. [CrossRef]
49. Katerinopolou, D.; Zalar, P.; Sweelssen, J.; Kiriakidis, G.; Rentorp, C.; Groen, P.; Gelinck, G.H.; van den Brand, J.; Smits, E.C.P. Large-area all-printed temperature sensing surfaces using novel composite thermistor materials. *Adv. Electron. Mater.* **2019**, *5*, 1800605. [CrossRef]
50. Kang, J.E.; Ryu, J.; Han, G.; Choi, J.J.; Yoon, W.H.; Hahn, B.D.; Kim, J.W.; Ahn, C.E.W.; Choi, J.H.; Park, D.S. $LaNiO_3$ conducting particle dispersed $NiMn_2O_4$ nanocomposite NTC thermistor thick films by aerosol deposition. *J. Alloys Compd.* **2012**, *534*, 70–73. [CrossRef]
51. Wang, C.; Hong, G.Y.; Li, K.M.; Yoon, H.T. A miniaturized nickel oxide thermistor via aerosol jet technology. *Sensors* **2017**, *17*, 2602. [CrossRef]
52. Schubert, M.; Kita, J.; Munch, C.; Moos, R. Analysis of the characteristics of thick-film NTC thermistor devices manufactured by screen-printing and firing technique and by room temperature aerosol deposition method. *Funct. Mater. Lett.* **2017**, *6*, 1750073. [CrossRef]
53. Li, H.; Zhang, H.; Chang, A.; Ma, X.; Rong, J.; Yang, L. A novel core-shell structure NTC ceramic with high stability fabricating by an in-situ ink-jet printing method. *J. Eur. Ceram. Soc.* **2021**, *41*, 4167–4174. [CrossRef]
54. Reimann, T.; Toepfer, J. Low temperature sintered Ni-Zn-Co-Mn-O spinel oxide ceramics for multilayer NTC thermistors. *J. Mater. Sci. Mater. Electron.* **2021**. [CrossRef]
55. Nikolic, M.V.; Krstic, J.B.; Labus, N.J.; Lukovic, M.D.; Dojcinovic, M.P.; Radovanovic, M.; Tadic, N.B. Structural, morphological and textural properties of iron manganite ($FeMnO_3$) thick films applied for humidity sensing. *Mater. Sci. Eng. B* **2020**, *257*, 114547. [CrossRef]
56. Nikolic, M.V.; Vasiljevic, Z.Z.; Lukovic, M.D.; Pavlovic, V.P.; Vujancevic, J.D.; Radovanovic, M.; Krstic, J.B.; Vlahovic, B.; Pavlovic, V.B. Humidity sensing properties of nanocrystalline pseudobrookite (Fe_2TiO_5) based thick films. *Sens. Actuators B* **2018**, *217*, 654–664. [CrossRef]
57. Selmi, M.; Smida, A.; Kossi, S.E. Effect of polaron formation in conduction and dielectric behavior in $La_{0.7}Sr_{0.25}K_{0.05}MnO_3$ oxide. *J. Mater. Sci. Mater. Electron.* **2021**, *32*, 6014–6027. [CrossRef]
58. Nikolic, M.V.; Sekulic, D.; Vasiljevic, Z.Z.; Lukovic, M.D.; Pavlovic, V.B.; Aleksic, O.S. Dielectric properties, complex impedance and electrical conductivity of Fe_2TiO_5 nanopowder compacts and bulk samples at elevated temperatures. *J. Mater. Sci. Mater. Electron.* **2017**, *28*, 4796–4806. [CrossRef]
59. Zhang, X.; Yao, S.; Zhao, D.; Liang, S. Nano-negative temperature coefficient thermistor with unique electrical properties of high B constant and low resistivity. *J. Mater. Sci. Mater. Electron.* **2021**, *32*, 5222–5232. [CrossRef]
60. Zhang, D.; Zong, X.; Wu, Z.; Zhang, Y. Ultrahigh-performance impedance humidity sensor based on layer-by-layer self-assembled tin disulfide/titanium dioxide nanohybrid film. *Sensors Actuators B Chem.* **2018**, *266*, 52–62. [CrossRef]
61. Pascariu, P.; Airinei, A.; Olaru, N.; Petrila, I.; Nica, V.; Sacarescu, L.; Tudorache, F. Microstructure, electrical and humidity sensor properties of electrospun NiO-SnO_2 nanofibers. *Sens. Actuators B* **2016**, *222*, 1024–1031. [CrossRef]
62. Bondarenko, A.S.; Ragoisha, G. EIS Spectrum Analyzer. Available online: https://www.abc.chemistry.bsu.by (accessed on 25 November 2016).
63. Ryu, J.; Park, S.S.; Schmidt, R. In-plane impedance spectroscopy in aerosol deposited $NiMn_2O_4$ negative temperature coefficient films. *J. Appl. Phys.* **2011**, *109*, 113722. [CrossRef]
64. Momma, K.; Izumi, F. VESTA 3 for three dimensional visualization of crystal, volumetric and morphology data. *J. Appl. Crystallogr.* **2011**, *44*, 1271–1276. [CrossRef]
65. Agmon, N. The Grotthuss charge mechanism. *Chem. Phys. Lett.* **1995**, *244*, 456–462. [CrossRef]